Two-dimensional shear wave speed and crawling wave speed recoveries from *in vitro* prostate data

Kui Lin[a)]
Westerngeco, 10001 Richmond Avenue, Houston, Texas 77042

Joyce R. McLaughlin and Ashley Thomas
Mathematical Sciences Department, Rensselaer Polytechnic Institute, Troy, New York 12180

Kevin Parker
Department of Electrical & Computer Engineering, University of Rochester, Rochester, New York 14627

Benjamin Castaneda
Medical Image Research Laboratory, Seccion Electricidad y Electronica, Departamento de Ingenieria, Pontificia Universidad Catolica del Peru, Lima, Peru

Deborah J. Rubens
Department of Imaging Sciences, University of Rochester Medical Center, Rochester, New York 14642

(Received 14 May 2010; revised 21 February 2011; accepted 10 May 2011)

The crawling wave experiment was developed to capture a shear wave induced moving interference pattern that is created by two harmonic vibration sources oscillating at different but almost the same frequencies. Using the vibration sonoelastography technique, the spectral variance image reveals a moving interference pattern. It has been shown that the speed of the moving interference pattern, i.e., the crawling wave speed, is proportional to the shear wave speed with a nonlinear factor. This factor can generate high-speed artifacts in the crawling wave speed images that do not actually correspond to increased stiffness. In this paper, an inverse algorithm is developed to reconstruct both the crawling wave speed and the shear wave speed using the phases of the crawling wave and the shear wave. The feature for the data is the application to *in vitro* prostate data, while the features for the algorithm include the following: (1) A directional filter is implemented to obtain a wave moving in only one direction; and (2) an L^1 minimization technique with physics inspired constraints is employed to calculate the phase of the crawling wave and to eliminate jump discontinuities from the phase of the shear wave. The algorithm is tested on *in vitro* prostate data measured at the Rochester Center for Biomedical Ultrasound and University of Rochester. Each aspect of the algorithm is shown to yield image improvement. The results demonstrate that the shear wave speed images can have less artifacts than the crawling wave images. Examples are presented where the shear wave speed recoveries have excellent agreement with histology results on the size, shape, and location of cancerous tissues in the glands. © *2011 Acoustical Society of America*. [DOI: 10.1121/1.3596472]

PACS number(s): 43.80.Qf, 43.20.Jr [PEB] Pages: 585–598

I. INTRODUCTION

Shear stiffness imaging of soft tissue arises from the importance of palpation in diagnosis where the presence of stiffer tissue is often an indicator of abnormality. As a noninvasive imaging technique, it can aim to quantitatively assess the shear stiffness parameter of soft tissue to identify tumor inclusions or can be used in an invasive procedure to guide, for example, needle insertion. In the experiments proposed so far, a variety of excitation methods have been developed to mechanically stimulate the tissue: (1) static compression, where the tissue is slowly compressed;[1–5,7] (2) harmonic oscillation, where up to two harmonic sources are used to create propagating shear waves;[8–17] and (3) transient pulses, where a traveling wave is created by a time-dependent point source or line source.[6,18–26] Once the tissue is excited, movies of the interior displacement tissue response are created by processing the data from successive ultrasound radio frequency/in phase and quadrature data acquisitions or successive magnetic resonance data acquisitions and images of displacement amplitude, or, using inverse algorithms, shear stiffness or shear wave speed are obtained.

Sonoelastography is a real-time imaging technique that uses Doppler ultrasound to capture the vibration pattern resulting from the propagation of low-frequency (less than 1 kHz) shear waves through internal organs.[14] In the single frequency vibration amplitude images of sonoelastography, local decrease in the peak vibration amplitude is associated with hard lesions in the uniform background and could be utilized to detect regions of abnormal stiffness. Vibroacoustography, on the other hand, is an imaging approach that uses dynamic radiation force to induce the acoustic response of deep tissue.[10,11] The localized radiation force is generated by two confocal continuous-wave ultrasound beams at frequencies that differ on the order of kilohertz. An acoustic

[a)]Author to whom correspondence should be addressed. Electronic mail: karl.linkui@gmail.com

signal in the kilohertz range is recorded near the body surface. The signal is proportional to shear wave speed in the region of the localized source. The speed is then imaged. What is different about vibroacoustography and the imaging modality that is the focus of this paper is that in vibroacoustography a shear wave speed image is created from a proportionality factor in a received acoustic signal created by interfering acoustic waves. Here two harmonic sources will produce an interference pattern created by two shear waves.

In this paper, we focus on the crawling wave experiment where two harmonic sources with slightly different frequencies are placed on the opposite sides of the domain.[16,17] The frequency difference is less than 1 Hz. So when the spectral variance is imaged by a Doppler ultrasound machine, a moving interference pattern is visualized. The scaled phase wave speed of the moving interference pattern has been imaged by either the Arrival Time algorithm[27] or the Kasai autocorrelator.[28,29] Although the crawling wave speed image can be scaled so that it is similar to a shear wave speed image in phantoms,[16,17,27] the relationship between the crawling wave speed and the shear wave speed has been shown to be nonlinear. This nonlinear relation could produce, especially in the case of point sources, high-speed artifacts in the images of scaled crawling wave speed that do not correspond to stiff inclusions in the images of shear wave speed.[30] In the case of line sources, however, the effect of the nonlinear relation between the scaled crawling wave speed and the shear wave speed is less. In this paper, we extend the results in Ref. 30 to *in vitro* prostate data generated by line sources (see Fig. 1 for the experimental setup) and develop a new inverse algorithm to reconstruct the scaled crawling wave speed and the shear wave speed from their individual phases. The algorithm utilizes a key concept relating the crawling wave phase, the crawling wave speed, and the shear wave phase and consists of five steps: (1) Filter the data to retain the crawling wave moving in one direction; (2) use a specialized optimization procedure (see Sec. III), which includes L^1 optimization with physically inspired constraints, to locally unwrap the phase of the crawling wave; (3) calculate the crawling wave speed by computing the phase derivatives of the unwrapped phase; (4) solve a first-order partial differential equation (PDE) for the phase of the shear wave induced by one of the sources; and (5) calculate the shear wave speed. To compare with the Arrival Time algorithm given in Ref. 30, we note that the above-mentioned steps (3), (4), and (5) are the same; it is steps (1) and (2) that are new. Since the new algorithm retains some features of the Arrival Time algorithm, we will refer to this new algorithm as AT.FL1.

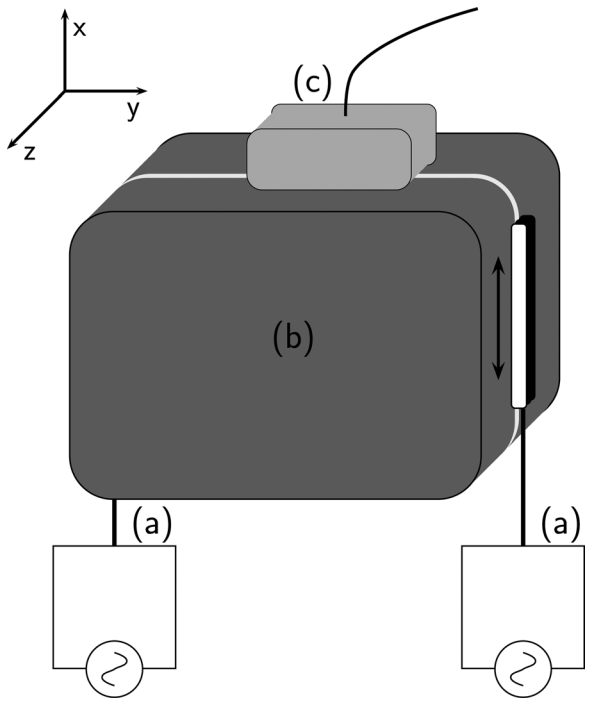

FIG. 1. Setup of the crawling wave experiment with two vibration bars as line sources: (a) shear vibration sources; (b) biomaterial; (c) ultrasound probe. The image plane is the cross section that is aligned with the two vibration bars and under the ultrasound probe. The boundary of the image plane is highlighted by the light gray curve. Vibration is in the direction of the black arrow, which is also the direction of the component of motion that can be measured.

From synthetic data generated by solving a two-dimensional visco-elastic acoustic wave equation with line sources, there is no need to filter the spectral variance data to obtain a wave moving in one direction. From laboratory *in vitro* prostate data, we do apply a filter to obtain a wave moving in one direction. The reconstruction results of the scaled crawling wave speed and the shear wave speed are presented to show that the shear wave speed recoveries can exhibit less artifacts than the scaled crawling wave speed recoveries. We show images to exhibit the improvement with each additional algorithmic feature.

Compared with the histology image, the shear wave speed images can have excellent agreement on the size, the shape, and the location of tumorous tissues in the gland, particularly when cutoffs are applied in image processing.

The remainder of this paper is organized as follows. In Sec. II we give a brief review of the mathematical models for forward and inverse problems. Section III is devoted to the development of our inverse algorithm. In Sec. IV we mention briefly our reconstruction results from simulated data. In Sec. V we give a description of the materials and methodology. Then Sec. VI presents numerical recoveries from *in vitro* prostate data. We end this paper in Sec. VII with concluding remarks and a discussion of future work.

II. MATHEMATICAL MODELS

A. Equations for the crawling wave speed and the shear wave speed

Here, we give a brief review of the mathematical formulations of equations for the crawling wave speed and shear wave speed. For more details, see. Refs. 27 and 30.

Assume the linear elastic model for the infinitesimal displacement induced by the vibration sources. The spectral variance, G^2, for the downward component of motion, which is the motion perpendicular to the transducer face and parallel to the vibration direction, is the imaged quantity in the crawling wave experiment. It can be written as

$$G^2 = |u+v|^2 = A^2 + B^2 + 2AB\cos(\omega_1\phi_1 + \omega_2\phi_2 - \Delta\omega t), \quad (1)$$

where $u(x,y,t) = Ae^{i\omega_1(t-\phi_1)}$, $v(x,y,t) = Be^{i\omega_2(-t-\phi_2)}$ are the downward time harmonic displacement responses in the imaging domain due to each of the two sources located on two sides of the medium. A and B are the amplitude of u and v. ϕ_1 and ϕ_2 are the corresponding phases. The crawling wave phase is defined to be $\hat{\Psi}(x,y) = \omega_1\phi_1(x,y) + \omega_2\phi_2(x,y)$, and can be extracted directly from the data. The crawling wave speed $c_{\hat{\Psi}}$ can then be calculated explicitly as it satisfies

$$c_{\hat{\Psi}}\left|\nabla\hat{\Psi}(x,y)\right| = \Delta\omega, \quad (2)$$

where $\Delta\omega = \omega_1 - \omega_2$. Here we assume that $\omega_1 > \omega_2$. The shear wave phase from each source, ϕ_1, ϕ_2, cannot be obtained from the data directly. At the same time, under a geometric optics approximation, those phases are directly related to the shear phase wave speed, c_s, by

$$c_s|\nabla\phi_1(x,y)| = c_s|\nabla\phi_2(x,y)| = 1. \quad (3)$$

Finally, $c_{\hat{\Psi}}$ is related to c_s as follows:

$$c_s = \frac{2\sqrt{\omega_1\omega_2}}{\Delta\omega}\left|\cos\left(\frac{\theta}{2}\right)\right| c_{\hat{\Psi}} + O\left(\frac{\Delta\omega}{\omega_1}\right), \quad (4)$$

where $\cos\theta = (\nabla\phi_1\cdot\nabla\phi_2)(|\nabla\phi_1|\cdot|\nabla\phi_2|)^{-1}$.

B. First-order PDE for the shear wave phase

The nonlinear scaling factor $\cos(\theta/2)$ in Eq. (4) is not necessarily equal to ± 1 in the case of point sources, as the two shear waves are not always propagating in exactly opposite directions even if the medium has a constant shear speed. In the case of two line sources, $|\cos(\theta/2)| = 1$ if the shear wave speed is constant in the domain. However, when the shear wave speed in the medium is not constant, the nonlinear scaling factor can be non-negligible.

In order to avoid possible artifacts in the images of crawling wave speed, we need to obtain one of the phases ϕ_1 or ϕ_2. A first-order PDE has been derived in Ref. 30 to compute the phases of the shear waves from the two sources:

$$\nabla\hat{\Psi}_1\cdot\nabla\phi_1 = \frac{(\Delta\omega)^2}{2\omega_1\omega_2 c_{\hat{\Psi}}^2} + O\left(\frac{\Delta\omega}{\omega_1}\right), \quad (5)$$

$$\nabla\hat{\Psi}_2\cdot\nabla\phi_2 = \frac{(\Delta\omega)^2}{2\omega_1\omega_2 c_{\hat{\Psi}}^2} + O\left(\frac{\Delta\omega}{\omega_1}\right), \quad (6)$$

where $\hat{\Psi}_1 = \hat{\Psi}/\omega_1$, $\hat{\Psi}_2 = \hat{\Psi}/\omega_2$. Note that we make this scaling so that the order of magnitude of $\hat{\Psi}_1$, $\hat{\Psi}_2$, ϕ_1, and ϕ_2 are similar. In the case of line sources, we can assume ϕ_1 is constant at one line source and ϕ_2 is constant at the other line source. Then either ϕ_1 or ϕ_2 can be calculated using Eq. (5) or Eq. (6) (neglecting the error term), and the shear wave speed can be computed from Eq. (3).

III. RECONSTRUCTION ALGORITHM

The algorithm to recover the crawling wave speed and the shear wave speed consists of five steps, which are discussed in detail in the following.

A. Step one: Directional filter

The mathematical formulations in Sec. II only consider the case where the shear wave from each source propagates through the medium and away from the source. This means that it does not model some reflections. However, in cases where there are stiff inclusions in the domain, the reflection of shear waves is inevitable. So while a movie of the crawling wave interference pattern appears to move in only one direction, the reflections from inclusions will influence the amplitude and phase of the imaged wave. In addition, when *in vitro* data are utilized, reflection may also occur at the interface between the prostate specimen and gels that surround the gland. In that case, the measured moving interference pattern would not be a single forward oscillating wave moving in one direction as it is assumed here and was previously assumed in Ref. 27.

Suppose now the shear waves propagating from the line sources on the left and the right sides of the domain are, respectively,

$$u_l = A_l e^{i\omega_1(\phi_1 - t)}, \qquad v_r = B_r e^{i\omega_2(-\phi_2 - t)}, \quad (7)$$

and the backward reflection of waves are, respectively,

$$u_r = A_r e^{i\omega_1(\tilde{\phi}_1 + t)}, \qquad v_l = B_l e^{i\omega_2(-\tilde{\phi}_2 + t)}. \quad (8)$$

Then the total waves from the left and right sources are, respectively,

$$u = u_l + u_r, \qquad v = v_l + v_r. \quad (9)$$

The spectral variance G^2 can be calculated from the following formula:

$$G^2 = |u+v|^2 = A_l^2 + A_r^2 + B_l^2 + B_r^2 + 2A_lA_r\cos\Psi_1 + 2B_lB_r\cos\Psi_2 + 2\Re(uv^*), \quad (10)$$

where $\Psi_1 = \omega_1(\tilde{\phi}_1 - \phi_1 + 2t)$, $\Psi_2 = \omega_1(\tilde{\phi}_2 - \phi_2 - 2t)$ If we remove the zero frequency term $A_l^2 + A_r^2 + B_l^2 + B_r^2$ and complexify (Hilbert transform in time) the rest of G^2, we will get

$$\hat{G}^2 = 2A_lB_re^{i(\omega_1\phi_1 + \omega_2\phi_2 - \Delta\omega t)} + 2A_rB_le^{i(\omega_1\tilde{\phi}_1 + \omega_2\tilde{\phi}_2 + \Delta\omega t)} + 2A_lB_le^{i(\omega_1\phi_1 + \omega_2\tilde{\phi}_2 - (\omega_1+\omega_2)t)} + 2A_lA_re^{i\Psi_1} + 2A_rB_re^{i(\omega_1\tilde{\phi}_1 + \omega_2\phi_2 + (\omega_1+\omega_2)t)} + 2B_lB_re^{i\Psi_2}. \quad (11)$$

As the sampling rate is only large enough to capture the changes in the spectral variance data at very low frequencies, e.g., $\Delta\omega$, the terms containing $A_lA_r, B_lB_r, A_lB_l, A_rB_r$ in the expression of $\hat{G}^2$ will be considered as high-frequency noise

in the data. The remaining part of $\hat{G}^2$ now contains two crawling waves of central frequency $\Delta\omega$ propagating in the opposite directions:

$$\hat{G}^2 = 2A_l B_r e^{i(\omega_1\phi_1+\omega_2\phi_2-\Delta\omega t)} + 2A_r B_l e^{i(\omega_1\tilde{\phi}_1+\omega_2\tilde{\phi}_2+\Delta\omega t)}. \quad (12)$$

Since the mathematical model and algorithms reviewed in Sec. II are designed to recover the wave speed of crawling waves moving in one direction, we need to separate those two waves. We accomplish this task by using a two-dimensional directional filter in time and the horizontal spatial variable on $\hat{G}^2$.

Suppose we take a two-dimensional Fourier transform in the horizontal space variable y and the time variable t of $\hat{G}^2$ at a fixed depth in the domain. In the k,ω frequency domain, the component of $\hat{G}^2$ moving from right to left is located in the first and third quadrants, while the left to right component is in the second and fourth quadrants as Fig. 2 shows. We remove all the frequency content in the first and third quadrants. Then we can inverse Fourier transform in k the remaining part, evaluate at $\Delta\omega$, and be left with the $\Delta\omega$ frequency content of the wave moving from left to right,

$$\hat{G}^2_{\text{filtered}} = A_l B_r e^{i(\omega_1\phi_1+\omega_2\phi_2)}. \quad (13)$$

B. Step two: L^1 minimization

It is straightforward to extract the wrapped phase of the crawling wave phase $\omega_1\phi_1+\omega_2\phi_2$. In order to eliminate the wrapped phase discontinuities at $-\pi$ and π and the effect of noise in the wrapped phase data, we employ a local phase unwrapping algorithm by using an L^1 minimization technique with physics inspired constraints. Our algorithm is inspired by the multilevel graph algorithm for two-dimensional phase unwrapping introduced in Ref. 31.

Suppose the wrapped phase from the complex data is $\Psi(x,y)$ and the target unwrapped phase is $\hat{\Psi}(x,y)$. Then,

$$\Psi(x,y) = \hat{\Psi}(x,y) + 2\pi k(x,y), \quad (14)$$

where $k(x,y)$ is an unknown integer function that forces $-\pi < \Psi \le \pi$. The goal here is to reconstruct $\hat{\Psi}(x,y)$ from $\Psi(x,y)$.

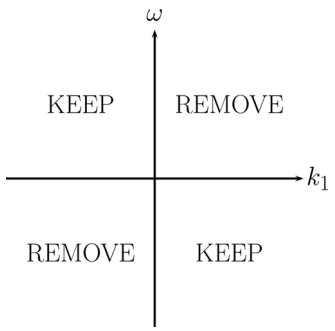

FIG. 2. Graphical illustration of two-dimensional filter.

The basic idea of our L^1 minimization technique is to minimize the distance between $\nabla\hat{\Psi}$ and the discrete gradient estimated from the values of the wrapped phase Ψ. On the two-dimensional grid (x_i,y_j), $1\le i\le m$, $1\le j\le n$ we first define the discrete gradient of Ψ as follows:

$$\Delta^x_{i,j} = W(\Psi_{i+1,j}-\Psi_{i,j}), \quad \Delta^y_{i,j} = W(\Psi_{i,j+1}-\Psi_{i,j}), \quad (15)$$

where $W(f_{i,j}) = f_{i,j} + 2\pi k_{i,j}$ with integer $k_{i,j}$ chosen such that $W(f_{i,j}) \in (-\pi,\pi]$. The wrapping operator W is introduced here as we expect the difference between values of the unwrapped phase at adjacent points should be within $\pm\pi$. We then require the grid-based solution $\hat{\Psi}_{i,j}$ to minimize the discrete functional

$$J = \sum_{i=1}^{m-1}\sum_{j=1}^{n} |\hat{\Psi}_{i+1,j}-\hat{\Psi}_{i,j}-\Delta^x_{i,j}| + \sum_{i=1}^{m}\sum_{j=1}^{n-1} |\hat{\Psi}_{i,j+1}-\hat{\Psi}_{i,j}-\Delta^y_{i,j}|. \quad (16)$$

To solve this nonlinear optimization problem with a linear programming technique, we change the minimization functional to a linear optimization problem by introducing two new variables $t_{i,j}, s_{i,j}$ and transforming the nonlinear objective value into linear constraints:

$$\begin{aligned} \min \quad & \sum_{i=1}^{m-1}\sum_{j=1}^{n} t_{i,j} + \sum_{i=1}^{m}\sum_{j=1}^{n-1} s_{i,j} \\ s.t. \quad & \text{for all } 1\le i\le m-1, \quad 1\le j\le n \\ & \begin{cases} \hat{\Psi}_{i+1,j}-\hat{\Psi}_{i,j}-\Delta^x_{i,j} \le t_{i,j} \\ \hat{\Psi}_{i+1,j}-\hat{\Psi}_{i,j}-\Delta^x_{i,j} \ge -t_{i,j} \end{cases} \\ & \text{for all } 1\le i\le m, \quad 1\le j\le n-1 \\ & \begin{cases} \hat{\Psi}_{i,j+1}-\hat{\Psi}_{i,j}-\Delta^y_{i,j} \le s_{i,j} \\ \hat{\Psi}_{i,j+1}-\hat{\Psi}_{i,j}-\Delta^y_{i,j} \ge -s_{i,j}. \end{cases} \end{aligned} \quad (17)$$

In addition to the self-imposed linear constraints, we further require: (1) $\hat{\Psi}_{i,j+1}-\hat{\Psi}_{i,j}\ge 0$; and (2) $|\hat{\Psi}_{i+1,j}-\hat{\Psi}_{i,j}| \le bd$, where bd is the mean of $|\Delta^x_{i,j}|$ over all i,j. The first set of constraints is inspired by the fact that the filtered crawling wave is only moving in one direction, and thus the phase of the wave should be monotonically increasing from the left side of the domain to the right side of the domain. The second set of the constraints is added to avoid phase jumps in the vertical direction. This can happen in areas with a low signal to noise ratio and result in low-speed artifacts in the images of phase wave speed recoveries.

With the additional linear constraints, the L^1 minimization problem that is solved for phase unwrapping is as follows:

$$\min \sum_{i=1}^{m-1}\sum_{j=1}^{n} t_{i,j} + \sum_{i=1}^{m}\sum_{j=1}^{n-1} s_{i,j}$$

$$s.t. \text{ for all } 1 \le i \le m-1, \quad 1 \le j \le n$$

$$\begin{cases} \hat{\Psi}_{i+1,j} - \hat{\Psi}_{i,j} - \Delta^x_{i,j} \le t_{i,j} \\ \hat{\Psi}_{i+1,j} - \hat{\Psi}_{i,j} - \Delta^x_{i,j} \ge -t_{i,j} \end{cases}$$

$$\text{for all } 1 \le i \le m, \quad 1 \le j \le n-1$$

$$\begin{cases} \hat{\Psi}_{i,j+1} - \hat{\Psi}_{i,j} - \Delta^y_{i,j} \le s_{i,j} \\ \hat{\Psi}_{i,j+1} - \hat{\Psi}_{i,j} - \Delta^y_{i,j} \ge -s_{i,j} \end{cases}$$

$$\text{for all } 1 \le i \le m, \quad 1 \le j \le n-1$$

$$\hat{\Psi}_{i,j+1} - \hat{\Psi}_{i,j} \ge 0$$

$$\text{for all } 1 \le i \le m-1, \quad 1 \le j \le n \tag{18}$$

$$\begin{cases} \hat{\Psi}_{i+1,j} - \hat{\Psi}_{i,j} \le bd, \\ \hat{\Psi}_{i+1,j} - \hat{\Psi}_{i,j} \ge -bd. \end{cases} \tag{19}$$

In our computations here, we utilize the MOSEK Optimization Software within MATLAB that provides specialized solvers for linear programming, mixed integer programming, and many types of nonlinear convex optimization problems.

Finally, an alternate method for locally unwrapping the phase is to apply a local cross correlation procedure:

1. At a specific point, (x_0, y_0) in the imaging domain, find the phase T_0 as the time shift that maximizes the cross correlation of the data $d(t, x_0, y_0)$ with an artificial reference signal $s(t)$:

$$T_0 = \arg\max_T \sum_k d(t_k, x_0, y_0) s(t_k - T).$$

The maximization problem is implemented by using the MATLAB command fminsearch to minimize the negative of the cross correlation function, using $T = 0$ as the starting value for the optimization method.

2. At each point (x, y) in a neighborhood of (x_0, y_0), compute the phase $T(x, y)$ as the time shift that maximizes the cross correlation of the data $d(t, x, y)$ with $s(t)$:

$$T(x, y) = \arg\max_T \sum_k d(t_k, x, y) s(t_k - T).$$

The maximization problem is again implemented using fminsearch, this time using $T = T_0$ as the starting value.

In Sec. VI we will compare the image quality when we use the L^1 algorithm in this paper to find the phase with the image quality when the phase is determined using local cross correlation.

C. Step three: Scaled crawling wave speed recovery

To compute the value of $\nabla\hat{\Psi}$ from the unwrapped phase, we utilize a two-dimensional averaging method to compute numerical derivatives.[32] Since the averaging method only requires values of unwrapped phase in a local window surrounding the point of interest, the L^1 phase unwrapping algorithm introduced in Sec. III B is performed locally in the averaging window. In this way, excess data noise in regions far away from the point of interest will not affect the phase unwrapping computation in the local averaging window. The implementation of this averaging algorithm that we used in our simulation studies[30] is valid when the spatial step sizes are equal to each other. In the case of *in vitro* data, the spatial step sizes dx and dy are different, so we explicitly show how the difference in discretization impacts the algorithm in this implementation of the averaging method:

$$\hat{\Psi}_{x,i,j} = \frac{1}{(2r_1+1)(2r_2+1)} \sum_{k=-r_1}^{r_1} \sum_{m=-r_2}^{r_2} \Psi^{m,k}_{x,i,j},$$

$$\Psi^{m,k}_{x,i,j} = \frac{\hat{\Psi}_{i+m+s_1,j+k} - \hat{\Psi}_{i+m-s_1,j+k}}{2s_1 dx}, \tag{20}$$

$$\hat{\Psi}_{y,i,j} = \frac{1}{(2r_3+1)(2r_4+1)} \sum_{k=-r_3}^{r_3} \sum_{m=-r_4}^{r_4} \Psi^{m,k}_{y,i,j},$$

$$\Psi^{m,k}_{y,i,j} = \frac{\hat{\Psi}_{i+k,j+m+s_2} - \hat{\Psi}_{i+k,j+m-s_2}}{2s_2 dy}, \tag{21}$$

where $r_2 < s_1, r_4 < s_2$. To choose the averaging parameters r_1, r_2, r_3, r_4, s_1 and s_2, we follow the general rule introduced in Ref. 32:

$$r_1 \sim r_2 \sim s_1 \sim O(dx^{-1/2}), \quad r_3 \sim r_4 \sim s_2 \sim O(dy^{-1/2}). \tag{22}$$

The range of the parameters that we have chosen yields excellent results in the numerical differentiation of $\hat{\Psi}$. However, making the optimal choice of the parameters still remains an important part of our future work.

After the phase derivatives are computed, the crawling wave speed is then computed by inverting Eq. (2) as

$$c_{\hat{\Psi}} = \frac{\Delta\omega}{|\nabla\hat{\Psi}|}. \tag{23}$$

Since the magnitude of the crawling wave speed is usually a small fraction of the shear wave speed, we image the scaled crawling wave speed

$$\frac{2\sqrt{\omega_1\omega_2}}{\Delta\omega} c_{\hat{\Psi}} \tag{24}$$

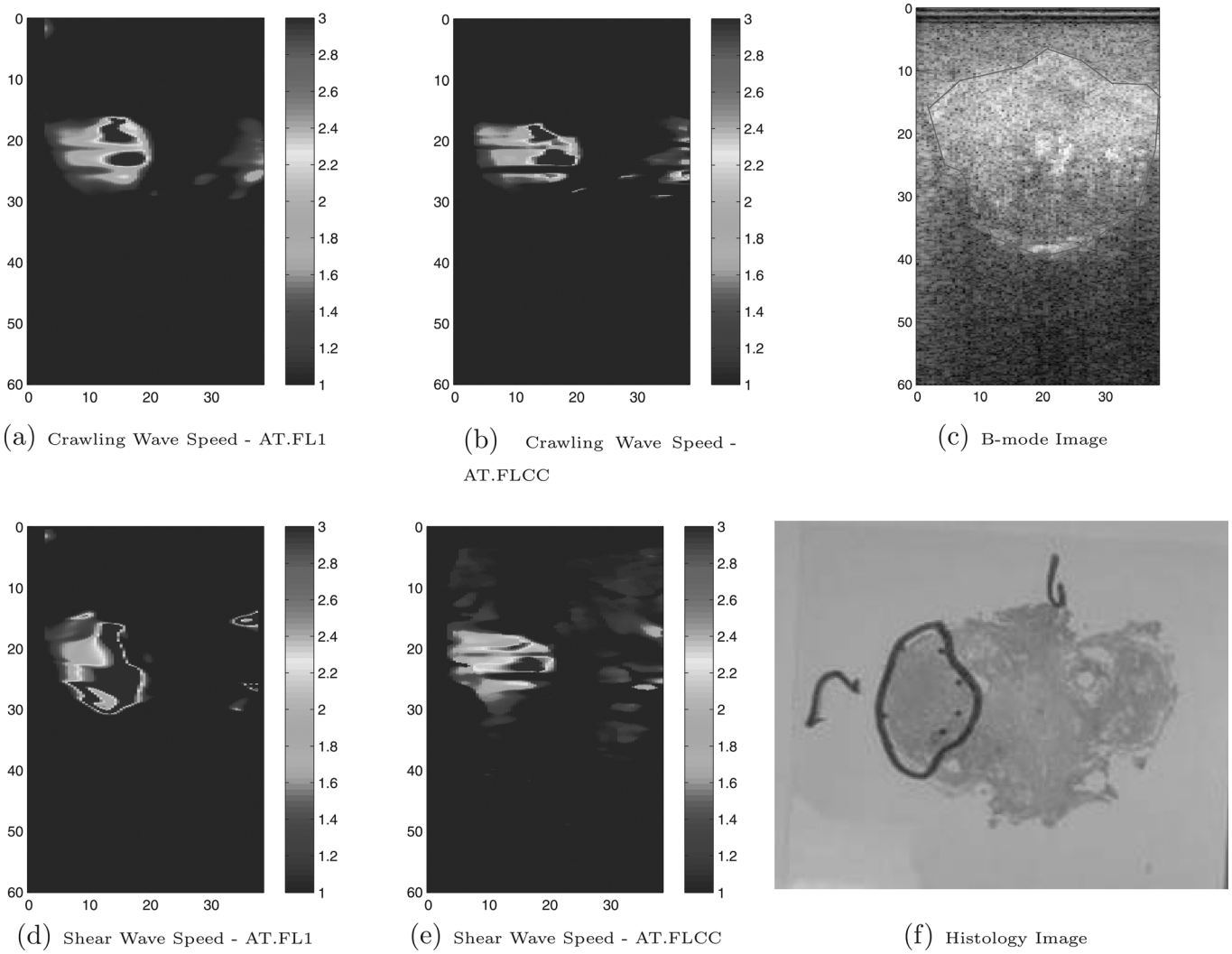

FIG. 3. Patient A: (a) Scaled crawling wave speed recovery with crawling wave phase identification using directional filter and L1 minimization: AT.FL1. (b) Scaled crawling wave speed recovery with crawling wave phase identification using directional filtering and local cross correlation: AT.FLCC. (c) *B*-mode image: The curve indicates the boundary of the prostate. (d), (e) Shear wave speed recoveries with crawling wave phase identification the same as in (a), (b). (f) Histology image: The black curve indicates the boundary of the tumor. Color bar for recoveries shown from 1 to 3 m/s.

to make a clearer comparison to the shear wave speed images.

D. Step four: Solving for the phase of shear wave

To get the phase ϕ_1 of the shear wave from the line source on the left side of the medium, we need to solve the first-order PDE (5):

$$\nabla\hat{\Psi}_1 \cdot \nabla\phi_1 = \frac{(\Delta\omega)^2}{2\omega_1\omega_2 c_{\hat{\Psi}}^2}. \tag{25}$$

In our previous work in the case of simulated data (see Ref. 30), this equation was solved by a first-order fully implicit marching scheme that is unconditionally stable. Here we adopt the same numerical solver for our inverse recoveries from simulated data and *in vitro* data.

E. Step five: Shear wave speed recovery

Before we use the two-dimensional averaging method to calculate the phase derivatives of the shear wave, the L^1 minimization procedure is applied again to eliminate jump discontinuities from the solution of the PDE and thus prevent nonphysical low-speed artifacts in the shear wave speed images. This step is usually not necessary throughout the whole domain. In some regions, when using laboratory data, it is needed.

So when this is needed, we solve the minimization problem (17)–(19), with $\hat{\Psi}$ replaced by ϕ_1. After we get ϕ_1 either from step (4) or from step (4) combined with an optimization procedure to remove jump discontinuities, we apply the averaging scheme (20) and (21) to compute $\nabla\phi_1$ and then obtain the shear wave speed using $c_s = |\nabla\phi_1|^{-1}$.

IV. WAVE SPEED RECOVERIES FROM SIMULATED DATA

The algorithm we present in this paper for recovering the scaled crawling wave speed and the shear wave speed is different from the one used in Ref. 30. However, if we use the same simulated data, the reconstructed images from both methods are similar. Note the model used for the simulations

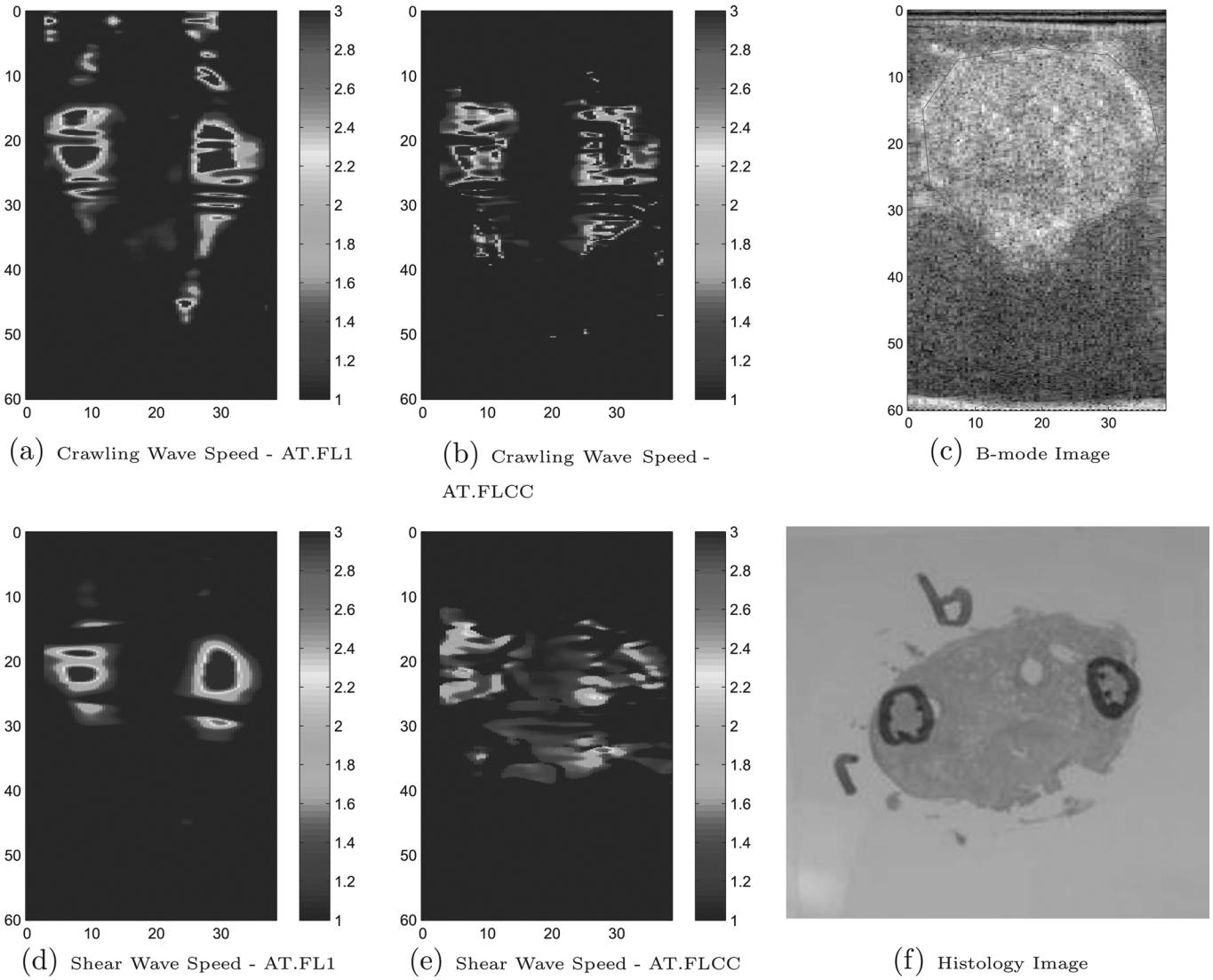

FIG. 4. Patient B: (a) Scaled crawling wave speed recovery with crawling wave phase identification using directional filter and L1 minimization: AT.FL1. (b) Scaled crawling wave speed recovery with crawling wave phase identification using directional filtering and local cross correlation: AT.FLCC. (c) *B*-mode image: The curve indicates the boundary of the prostate. (d), (e) Shear wave speed recoveries with crawling wave phase identification the same as in (a), (b). (f) Histology image: The black curve indicates the boundary of the tumor. Color bar for recoveries shown from 1 to 3 m/s.

contains viscoelastic effects and is a two-dimensional model (see Ref. 30). On the other hand, for *in vitro* data where viscoelastic effects and measurement instrument effects are present, the L^1 optimization procedure resulted in significant improvement in image quality (see Sec. VI).

V. MATERIALS AND METHODS

The *in vitro* prostate data that we used in this paper were obtained at the Rochester Center for Biomedical Ultrasound. The *in vitro* cases involving human prostate glands presented in this study were approved by the Institutional Review Board of the University of Rochester Medical Center and the Institutional Review Board of Rensselaer Polytechnic Institute. The *in vitro* cases are also compliant with the Health Insurance Portability and Accountability Act. In all cases, it was verified that the patient was not treated with radiation or hormonal therapies or with chemotherapy which alter the gland stiffness and the amount of residual tumor. In the five cases examined, the age of the patients ranged from 59 to 62 years with an average of 60 years. All of the patients presented adenocarcinomas confirmed with histology. Two of them had a Gleason score of 6 and the others had a Gleason score of 7.

Following radical prostatectomy, five prostatic glands were obtained and then embedded in a 10.5% gelatin mold. Three cross sections: AB1 (close to the apex), AB2 (at middle gland), and AB3 (close to the base) were selected from each gland to be imaged at approximately 10, 20, and 30 mm from the apex. Shear vibration was created in the medium by two pistons (model 2706, Bruel Kjaer, Naerum, Denmark) with surface-abraded extensions at the opposite sides of the gelatin mold (see Fig. 1). The vibration sources were moved to match the position of each imaged cross section. Crawling wave data were obtained with a GE LOGIQ 9 ultrasound transducer (M12L, General Electric Healthcare, Milwaukee, WI) that is positioned equidistant from the vibration sources and on top of the gelatin mold (see Fig. 1).

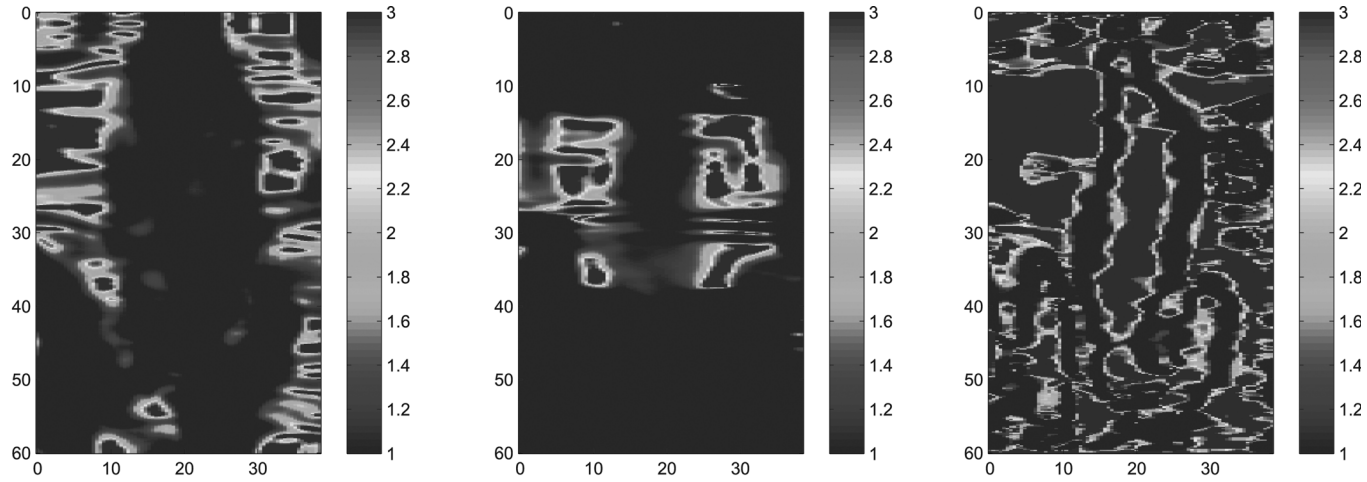

(a) Crawling Wave Speed - AT.FL1 with physical constraints and no Directional Filter

(b) Crawling Wave Speed - AT.FL1 with directional filter and no Physical Constraints

(c) Crawling Wave Speed - local cross correlation with no directional filter

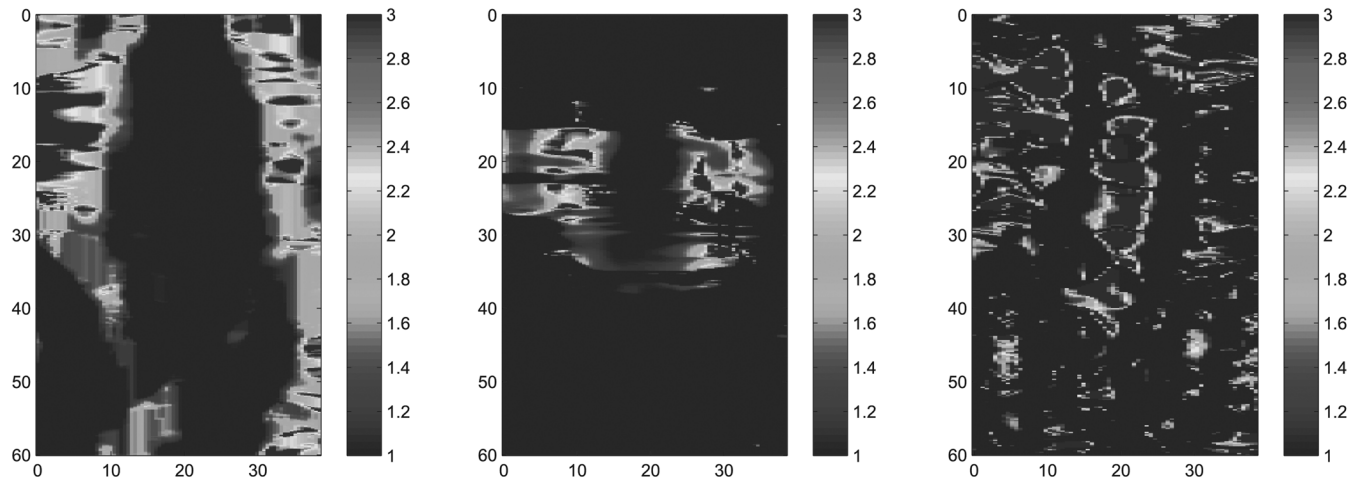

(d) Shear Wave Speed - AT.FL1 with physical constraints and no Directional Filter

(e) Shear Wave Speed - AT.FL1 with directional filter and no Physical Constraints

(f) Shear Wave Speed - local cross correlation with no directional filter

FIG. 5. Patient B: (a) Scaled crawling wave speed recovery: L1 minimization with physical constraints and no directional filtering. (b) Scaled crawling wave speed recovery: L1 minimization with directional filtering and no physical constraints. (d), (e) Shear wave speed recoveries with crawling wave phase identification as in (a), (b), respectively. (c), (f) Scaled crawling wave speed and shear wave speed images using local cross correlation for the crawling wave phase identification with no directional filter. Color bar for recoveries shown from 1 to 3 m/s.

The frequencies for *B*-mode and Doppler US were set to 9 and 5 MHz, respectively. The focus depth for the Doppler US acquisition was set to approximately three quarters of the gland. The sampling rate was 10 frames/s. For each cross section, three sets of moving interference data were obtained with three different vibration frequencies (100, 120, and 140 Hz). These frequencies were selected as a compromise between resolution and attenuation. Higher frequencies did not provide good penetration, especially at the base of the gland. The frequency offset between the two vibration sources was 0.25 Hz in all cases. This offset allowed for a visual feedback in the screen of the US scanner to provide a sense of the quality of the images acquired. This feature enabled avoiding cine loops in which waves were not propagating from one side of the imaging plane to the other as expected. One data set was collected for each cross section and each frequency (nine cine loops per patient). After imaging, a needle was inserted into the gland using *B*-mode guidance to mark the position for later pathological processing.

For each prostatic specimen, the histological slices were obtained from the corresponding cross sections (marked with a needle) and the cancerous regions in the histological slices were outlined by an expert pathologist to serve as the true identifier of tumor size and location. The pathologist was blinded to the imaging results. Other normal glandular prostate features, including BPH, were not marked in the specimens so our imaging results focus on tumor identification.

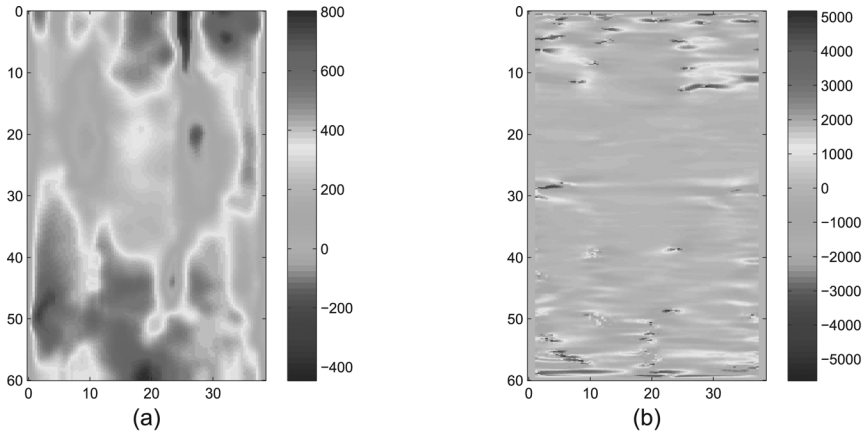

(a) Crawling Wave Phase Derivative $\hat{\psi}_y$ - AT.FL1 (b) Crawling Wave Phase Derivative $\hat{\psi}_y$ - AT.FLCC

FIG. 6. Patient B: (a) Crawling wave phase derivative, $\hat{\Psi}_y$, when Ψ is obtained by directional filter and L1 minimization with physical constraints. (b) Crawling wave phase derivative, $\hat{\Psi}_y$, when $\hat{\Psi}$ is obtained by directional filter and local cross correlation.

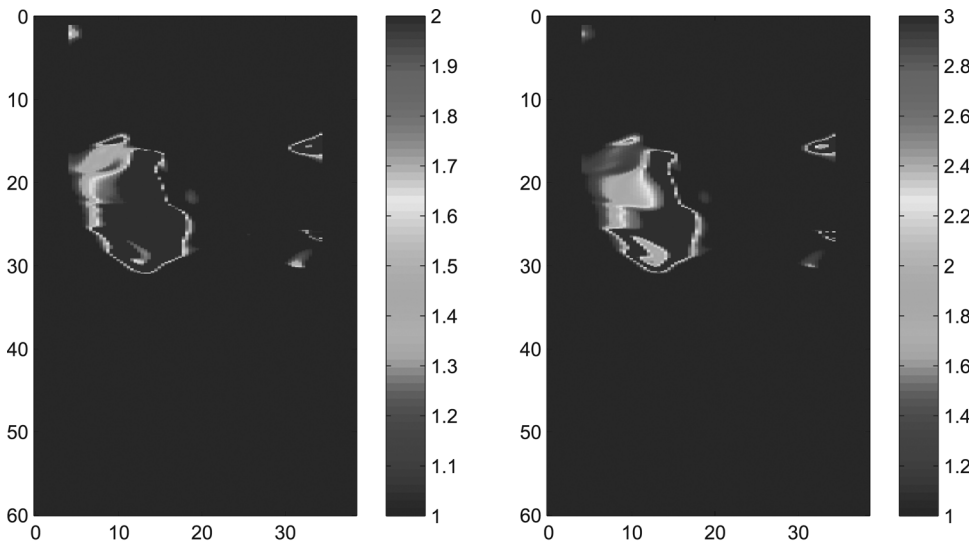

(a) Shear Wave Speed (b) Shear Wave Speed

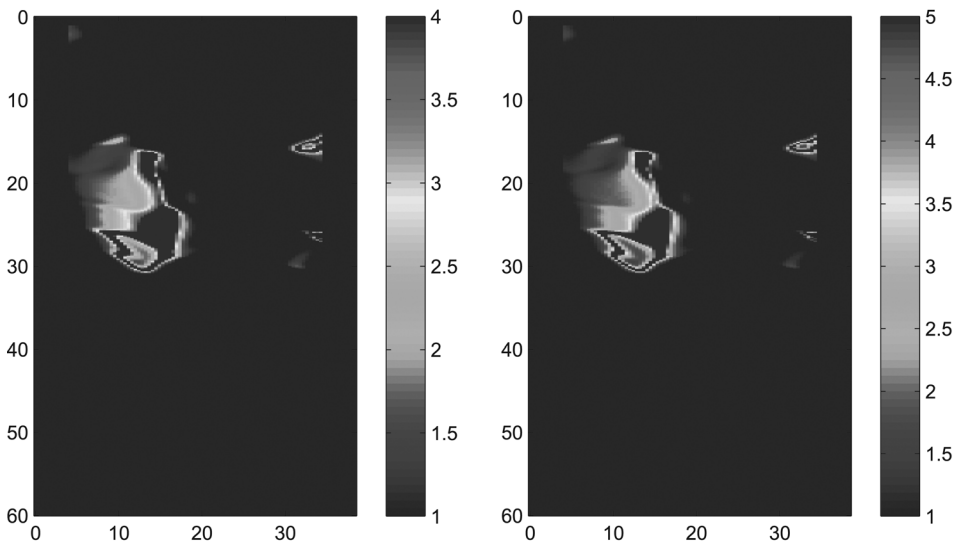

(c) Shear Wave Speed (d) Shear Wave Speed

FIG. 7. Patient A's shear wave speed images: (a) with the upper cutoff of 2 m/s; (b) with the upper cutoff of 3 m/s; (c) with the upper cutoff of 4 m/s; and (d) with the upper cutoff of 5 m/s.

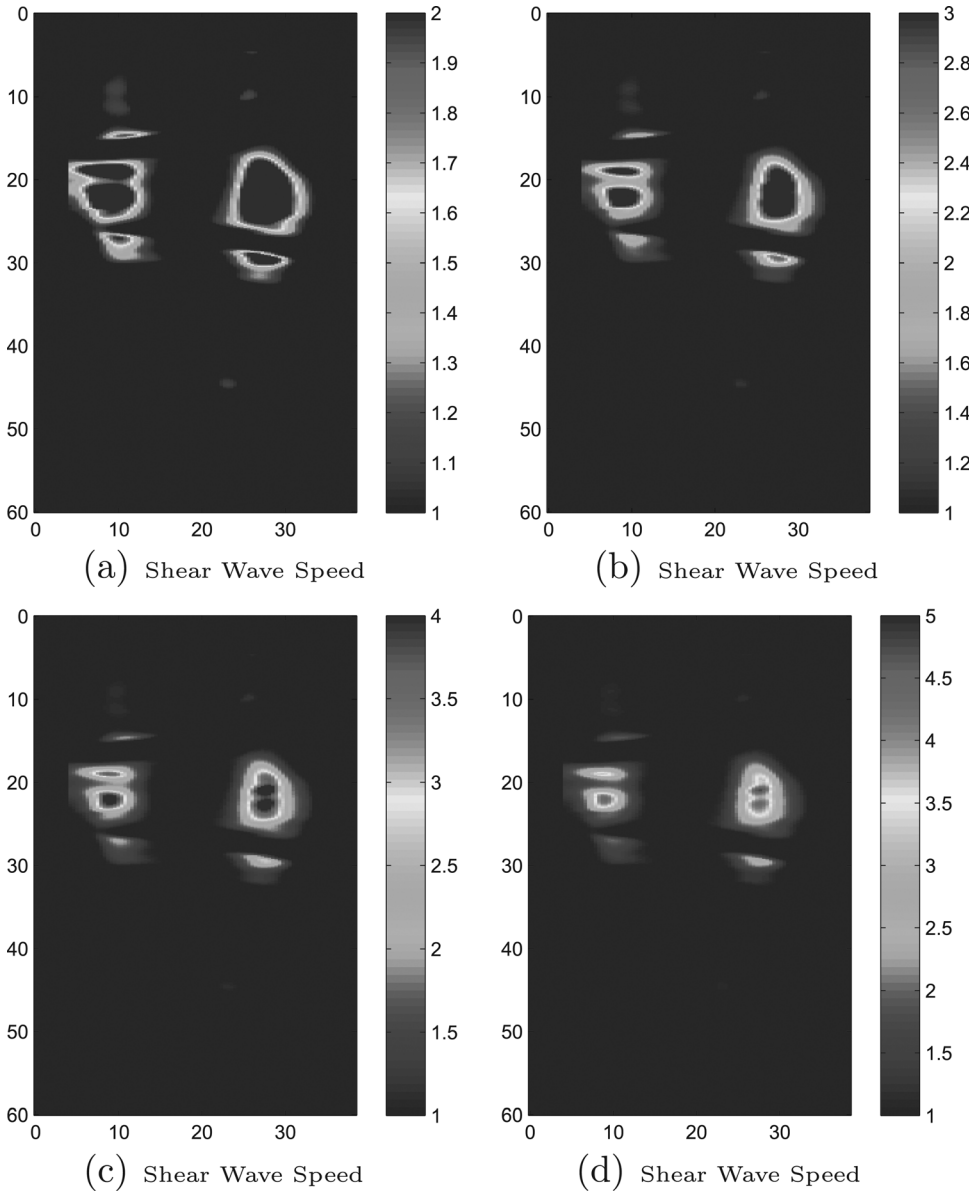

FIG. 8. Patient B's shear wave speed images with upper cutoffs: (a) 2 m/s; (b) 3 m/s; (c) 4 m/s; and (d) 5 m/s.

VI. WAVE SPEED RECOVERIES FROM *IN VITRO* PROSTATE DATA

Here, we show a few examples to demonstrate our results on *in vitro* data. We demonstrate the scaled crawling wave speed and shear wave speed recoveries from *in vitro* prostate data by using (1) the inverse algorithm introduced in Sec. II; (2) replacing the second step in the algorithm in Sec. III by the local cross correlation method; (3) showing how the images deteriorate as each step of the algorithm is either removed or replaced by another method; (4) showing that a total variation metric increases as steps in the algorithm are removed or replaced by an alternate method; (5) exhibiting the difference in phase derivatives when the phase is identified by our L^1 optimization method and when the phase is identified by local cross correlation and directional filtering; and (6) exhibiting the effect of the upper cutoff. For our examples, we chose one cross section, and one frequency, per patient. For the cross sections that correspond to patients A and B, extensive demonstration of the effect of the new algorithm on shear wave speed images is given as described in (2)–(6). In these images, using the new algorithm, there are no significant artifacts. For completeness, we include an image for a cross section for patients C and D; in each case a high-speed artifact, which is in the gel outside of the prostate, is present. We do not add an image for the remaining patient; there the prostate was located at the bottom of the container and the data quality was significantly reduced as compared to the data for the other four patients.

Figure 3 illustrates the scaled crawling wave speed image, the shear wave speed image, the corresponding *B*-mode image, and the matched histology image for patient A using the new algorithm that we designated by AT.FL1. In addition, we display the images of the scaled crawling wave speed and the shear wave speed when the phase is identified by directional filtering and local cross correlation.[30] To distinguish this[30] from other versions of the Arrival Time algorithm, we denote the algorithm using local cross correlation by AT.FLCC. So for the images in Fig. 3, the scaled crawling wave phase is

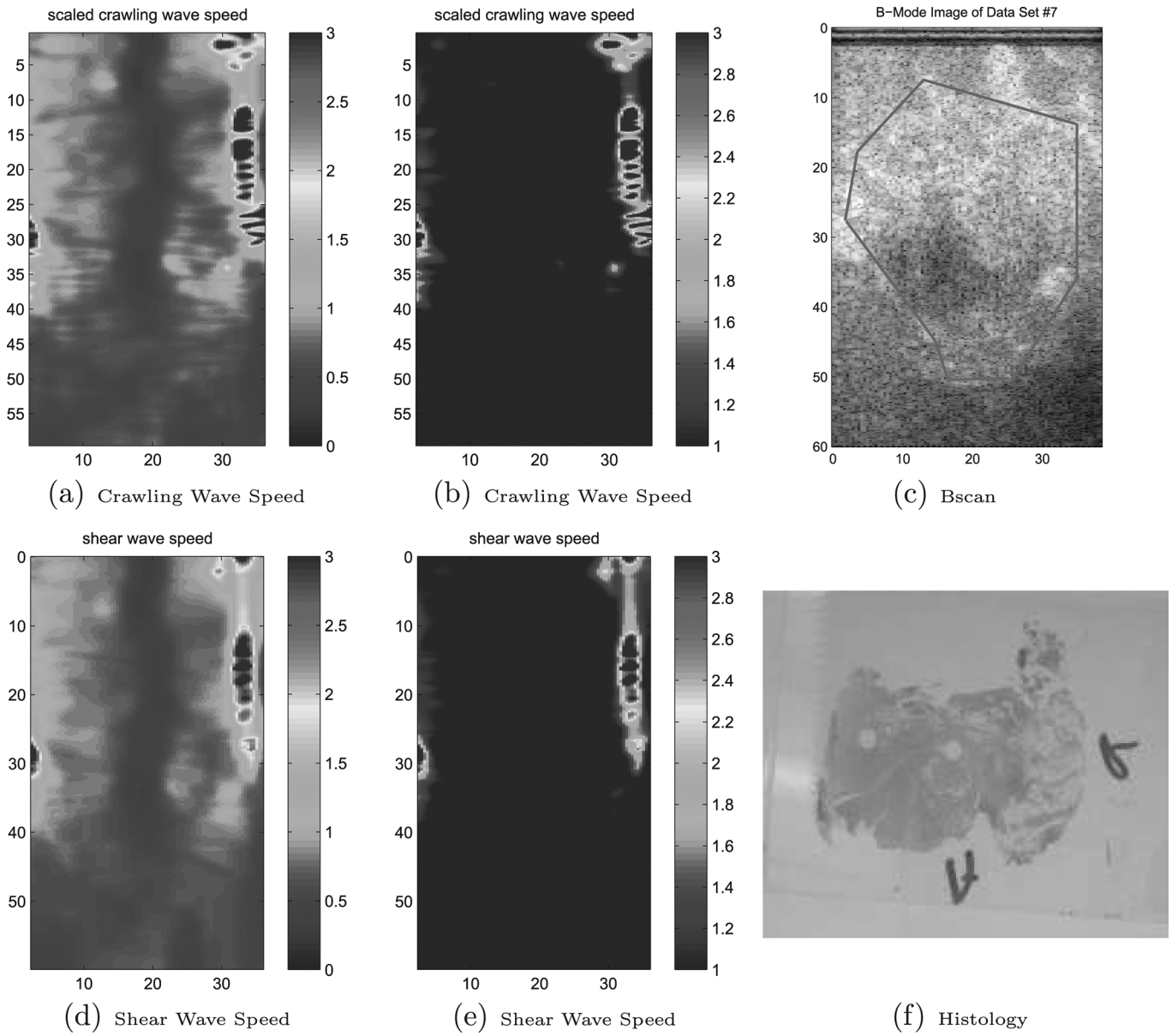

FIG. 9. Patient C: (a), (b) Scaled crawling wave speed with no lower cutoff and lower cutoff set to 1. (d), (e) Shear wave speed with no lower cutoff and lower cutoff set to 1. (c) *B* scan. (f) Histology slide. In this case there are artifacts in the gel outside the prostate.

determined either by using the local L^1 optimization technique and directional filtering or by local cross correlation and directional filtering. For this data set, the two-bar vibration sources are at frequencies 100 and 100.25 Hz. Notice that both the scaled crawling wave speed recovery and the shear wave speed recovery capture a distinct region in the left gland of elevated velocity. There is no corresponding dark irregular shaped region visualized on the *B*-mode ultrasound image. However, when the shear wave speed image is compared with the histology result, the shear velocity image clearly has agreement with the size, location, and the shape of the cancerous tissue. In addition, the scaled crawling wave phase derivatives obtained with filtering and local cross correlation phase identification are noiser than the phase derivatives obtained with filtering and local L^1 optimization phase unwrapping. Thus local cross correlation results in less accurate shear wave phase when solving the first-order partial differential equation (5). Comparing the shear wave speed images in Fig. 3, the result obtained with filtering and the L^1 phase unwrapping algorithm provides significant improvement on the identification of the size and location of the cancerous tissue over the result obtained when using filtering and local cross correlation. Note that the histology report shows that there is an adenocarcinoma close to the apex.

In Fig. 4 we demonstrate reconstruction results for patient B. In this case, the two-bar vibration sources are at frequencies 120 and 120.25 Hz. The histology result illustrates two tumors (adenocarcinomas) of size 4 mm in diameter in the gland, both of which are captured by our wave speed recoveries. Here, for two images we use directional filtering and the L^1 optimization step presented in this paper and for two additional images we use local cross correlation and directional filtering to recover the scaled crawling wave phase. Comparing Figs. 4(a) and 4(d), the shear wave speed image has fewer artifacts than the scaled crawling wave

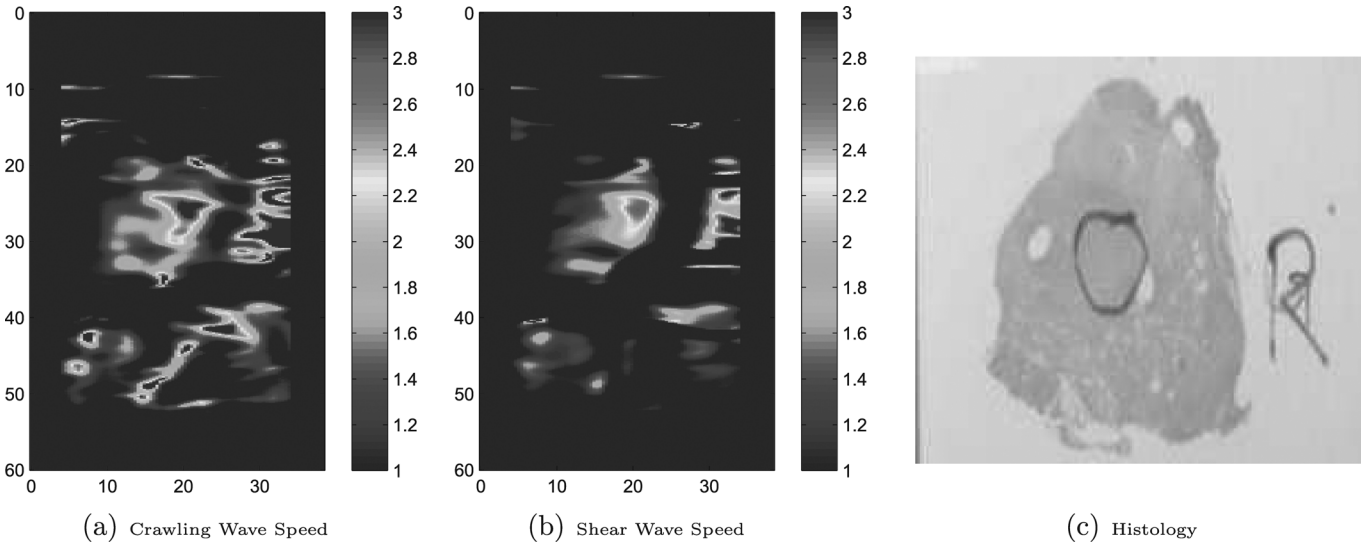

FIG. 10. Patient D: (a) Scaled crawling wave speed; (b) shear wave speed; and (c) histology slide. These images are for the fourth patient. The stiff region in the center of the image corresponds to the area marked in the histology slide. There is an artifact on the right of the shear wave speed image that is located in the gel outside of the prostate.

speed image and the edge of the lesions is also smoother in the shear wave speed image. For this data set, the shear wave speed image obtained with directional filtering and the L^1 optimization crawling wave phase unwrapping algorithm visually gives a better definition on the size and the location of cancerous tissue. The directional filtering and local cross correlation crawling wave phase identification step errors ultimately result in an image that poorly correlates with the histology markings.

To demonstrate the benefits of the directional filter and the physics inspired constraints in the L^1 minimization procedure, we present in Fig. 5 the scaled crawling wave speed and shear wave speed recoveries obtained using the following three algorithmic combinations for the crawling wave phase identification for patient B: (1) L^1 optimization with physics inspired constraints but without the directional filter; (2) L^1 optimization with the directional filter but without physics inspired constraints; and (3) local cross correlation without the directional filter. The results obtained with any of these changes are clearly inferior to the results shown in Fig. 4. To further quantify the difference of the image quality, we computed the total variation of the phase wave speed recovery given in Fig. 4(a) and Figs. 5(a)–5(c) using the following formula:

$$\mathrm{TV} = \sum_{i=1}^{m-1}\sum_{j=1}^{n} |\mathrm{sp}_{i+1,j} - \mathrm{sp}_{i,j}| + \sum_{i=1}^{m}\sum_{j=1}^{n-1} |\mathrm{sp}_{i,j} - \mathrm{sp}_{i,j+1}|,$$

where sp denotes the wave speed recovery. The value of the total variation is $5.32\mathrm{E}+3$ for the result given by AT.FL1 and $1.83\mathrm{E}+4$, $8.99\mathrm{E}+3$, and $1.6446\mathrm{E}+5$ for the results obtained with the algorithmic changes (1), (2), and (3), which correlates very well with the visual comparison.

For patient B we compare the crawling wave phase derivative, $\hat{\Psi}_y$, where the phase is determined by the directional filtering together with the L^1 minimization technique and the same crawling wave phase derivative, where the phase is determined by the local cross correlation and the directional filtering. From Fig. 6, the derivative, $\hat{\Psi}_y$, from the directional filtering and the L^1 algorithm shows fewer jump discontinuities than that obtained with the directional filtering and local cross correlation.

In Figs. 7 and 8 we present images of shear wave speed with different upper cutoff values for patients A and B. Notice that the location of the stiffness regions does not change and the size of the regions is similar. There is always a trade-off when choosing the color bar for the images. To exhibit this in our particular case, we choose a slice for patient C where there is no cancer. In Fig. 9 we show the effect of the lower cutoff. In this case the two-bar vibration sources are at frequencies 140 and 140.25 Hz. We show images with no lower cutoff and images with the lower cutoff set at 1. This shows that when we use the lower cutoff in order to emphasize the contrast between normal prostate and cancerous prostate, the variation of the speeds in the normal prostate, even the variations above 1, are more difficult to discern.

For completeness, in Fig. 10 we show the scaled crawling wave speed and shear wave speed images, along with the histology slide image for patient D. In this case, the two-bar vibration sources are at frequencies 100 and 100.25 Hz. Here the algorithm correctly identifies the cancerous region in the middle of the prostate as a high-speed region. However, there is also a high-speed artifact at the far right of the image. This artifact is located outside of the prostate in the gel.

VII. CONCLUSION AND DISCUSSION

In this paper, we have developed an algorithm to image the speed of the moving interference patterns and the speed of the shear wave from their individual phases in the crawling wave experiment and have applied the new method to *in vitro* prostate data. The inversion method includes a new concept. There are two new features of our algorithm

designed to remove the reflected wave, to minimize the effect of noise in the data, and to reduce the amount of nonphysical low-speed artifacts in the images: (1) a directional filter to obtain a wave moving in only one direction; and (2) an L^1 minimization technique with physics inspired constraints to calculate the phase of the crawling wave and to eliminate jump discontinuities from the phase of the shear wave. The reconstruction results of wave speed from simulation studies are qualitatively the same as reconstructed by Ref. 30 and exhibit only a small difference between the scaled crawling wave speed image and the shear wave speed image when the vibration excitations are line sources. So we have not presented those results here. However, the application of our inverse algorithm presented in this paper to the *in vitro* prostate data shows that the shear wave speed images can exhibit less artifacts and can capture the shape of the cancerous lesions better than the scaled crawling wave speed images.

Several procedures in the inverse algorithm and the simulation study could be improved for future applications:

- We introduced a set of physics inspired constraint (8) in order to eliminate low-speed artifacts from the scaled crawling wave speed images. The upper bound parameter *bd* is chosen as the mean value of the targeted phase vertical difference $|\Delta^x_{i,j}|$. This bound is introduced based on the observation that $|\Delta^x_{i,j}|$ has significant amplitude only in very limited regions of the image plane. Thus, using the average of $|\Delta^x_{i,j}|$ as the upper bound of phase change can prevent a jump discontinuity in the unwrapped phase $\hat{\Psi}$. However, this method is a global approach, which gives equal weight to all the points in the medium, inside or outside of the prostate specimen. We could very well focus on those limited regions where the signal to noise ratio (SNR) is low to choose a better upper bound on the vertical phase change to improve the quality of our images.
- The upper cutoff of the reconstruction results presented in Sec. VI is plotted with the color bar cut off at 3 m/s. Different cutoff values result in slightly different outlines of the cancerous lesions in the two-dimensional plot but the location of the cancerous tissue is unchanged. The effect of the upper cutoffs is exhibited in Figs. 7 and 8. A more rigorous approach to choose the upper cutoff value could be adopted to exhibit the best edge detection of the lesions. This approach is beyond the scope of this paper. The lower cutoff value we use here is 1.4 times the average value in a quadrant of normal prostate tissue. This is chosen since we target imaging tissue that is stiffer than normal tissue average values. We recognize that choosing a lower cutoff which is greater than 0 can mask the variations in the normal prostate. We demonstrate this in Fig. 9. A more rigorous approach to determine the optimal lower bound that also allows a clearer view of normal prostate features could be adopted. This approach too is beyond the scope of this paper.
- In this paper, we perform a directional filter on the crawling wave spectral variance with the goal to remove the backscatter. This produced images that displayed good agreement with histology results. It remains to complete a study to obtain an optimal filter to capture the richest data set from which diagnostically useful biomechanical images can be reconstructed.

ACKNOWLEDGMENTS

The authors acknowledge partial funding from the following: ONR Grants Nos. N000 14-05-1-0600, N000 14-08-1-0432, and NIA Grant No. R01AG029804. The authors would like to thank Dr. Christopher Hazard, Dr. Kai E. Thomenius at GE R & D, Dr. Antoinette M. Maniatty and Dr. Assad A. Oberai in MANE of RPI for useful discussions. The authors also thank Dr. Jorge Yao, M.C. for providing his expertise in pathology. J.R.M. and A.T. benefited from their visit during the Inverse Problems special program at the Mathematical Sciences Research Institute (MRSI), Berkeley, CA.

[1]P. E. Barbone and J. C. Bamber, "Quantitative elasticity imaging: What can and cannot be inferred from strain images," Phys. Med. Biol. **47**, 2147–2164 (2002).
[2]E. E. Konafagou, T. Harrigan, and J. Ophir, "Shear strain estimation and lesion mobility assesment in elastography," Ultrasonics **38**, 400–404 (2000).
[3]A. N. Oberai, M. D. Gokhale, and J. Bamber, "Evaluation of the adjoint equation based algorithm for elasticity imaging," Phys. Med. Biol. **49**, 2955–2974 (2004).
[4]M. O'Donnell, A. R. Skovoroda, B. M. Shapo, and S. Y. Emelianov, "Internal displacement and strain imaging using ultrasonic speckle tracking," IEEE Trans. Ultrason. Ferroelectr. Freq. Control **41**, 314–325 (1994).
[5]J. Ophir, E. I. Céspedes, H. Ponnekanti, Y. Yazdi, and X. Li, "Elastography: A quantitative method for imaging the elasticity of biological tissue," Ultrason. Imaging **13**, 111–134 (1991).
[6]T. Sugimoto, S. Ueha, and K. Itoh, "Tissue hardness measurement using the radiation force of focused ultrasound," Proc IEEE Ultrason. Symp. **1**, 1377–1380 (1990).
[7]A. Thitaikumar and J. Ophir, "Effect of lesion boundary conditions on axial strain elastograms: A parametric study," Ultrasound Med. Biol. **33**, 1463–1467 (2007).
[8]L. Curiel, R. Souchon, O. Rouviere, A. Gelet, and J. Y. Chapelon, "Elastography for the follow-up of high-intensity focused ultrasound prostate cancer treatment: Initial comparison with mri," Ultrasound Med. Biol. **31**, 1461–1468 (2005).
[9]R. L. Ehman, A. Manducca, J. R. McLaughlin, D. Renzi, and J.-R. Yoon, "Variance controlled shear stiffness images for MRE data," *IEEE International Symposium on Biomedical Imaging: Macro to Nano*, 2006, pp. 960–963.
[10]M. Fatemi and J. F. Greenleaf, "Ultrasound-stimulated vibro-acoustic spectrography," Science **280**, 82–85 (1998).
[11]J. Greenleaf, M. Fatemi, and M. Insana, "Selected methods for imaging elastic properties of biological tissues," Annu. Rev. Biomed. Eng. **5**, 57–58 (2003).
[12]C. Maleke, J. Luo, and E.E. Konofagou, "2d simulation of the amplitude-modulated harmonic motion imaging (am-hmi) with experimental validation," *IEEE International Ultrasonics Symposium*, 2007, pp. 681–706.
[13]A. Manduca, D. S. Lake, and R. L. Ehman, "Improved inversion of mr elastography images by spatio-temporal directional filtering," Proc. SPIE **5032**, 445–452 (2003).
[14]K. J. Parker, D. Fu, S. M. Gracewski, F. Yeung, and S. F. Levinson, "Vibration sonoelastography and the detectability of lesions," Ultrasound Med. Biol. **24**, 1937–1947 (1988).
[15]R. Sinkus, K. Siegmann, T. Xydeas, M. Tanter, C. Claussen, and M. Fink, "Mr elastography of breast lesions: Understanding the solid/liquid duality can improve the specificity of contrast-enhanced MR mammography," Magn. Reson. Med. **58**, 1135–1144 (2007).
[16]Z. Wu, D. J. Rubens, and K. J. Parker, "Sonoelastographic imaging of interference patterns for estimation of the shear velocity distribution in biomaterials," J. Acoust. Soc. Am. **120**, 535–545 (2006).
[17]Z. Wu, L. S. Taylor, D. J. Rubens, and K. J. Parker, "Sonoelastographic imaging of interference patterns for estimation of the shear velocity of homogeneous biomaterials," Phys. Med. Biol. **49**, 911–922 (2004).

[18]J. Bercoff, M. Tanter, and M. Fink, "Supersonic shear imaging: A new technique for soft tissue elasticity mapping," IEEE Trans. Ultrason. Ferroelectr. Freq. Control **19**, 396–409 (2004).
[19]S. Chen, M. W. Urban, C. Pislaru, R. Kinnick, Y. Zheng, A. Yao, and J. F. Greenleaf, "Shearwave dispersion ultrasound vibrometry (sduv) for measuring tissue elasticity and viscosity," IEEE Trans. Ultrason. Ferroelectr. Freq. Control. **56**, 55–62 (2009).
[20]K. R. Nightingale, S. A. McAleavey, and G. E.Trahey, "Shear wave generation using acoustic radiation force: In vivo and ex vivo results," Ultrasound Med. Biol. **29**, 171501723 (2003).
[21]M. L. Palmeri, J. J. Dahl, D. B. Macleod, S. A. Grant, and K. R. Nightingale, "On the feasibility of imaging peripheral nerves using acoustic radiation force impulse imaging," Ultrasound Imaging **31**, 172–182 (2009).
[22]M. L. Palmeri, S. A. McAleavey, G. E. Trahey, and K. R. Nightingale, "Ultrasonic tracking of acoustic radiation force-induced displacements in homogeneous media," IEEE Trans. Ultrason. Ferroelectr. Freq. Control **53**, 1300–1313 (2006).
[23]M. L. Palmeri, M. H. Wang, J. J. Dahl, K. D. Frinkley, and K. R. Nightingale, "Quantifying hepatic shear modulus in vivo using acoustic radiation force," Ultrasound Med. Biol. **34**, 546–558 (2008).
[24]L. Sandrin, M. Tanter, S. Catheline, and M. Fink, "Shear modulus imaging with 2-d transient elastography," IEEE Trans.Ultrason. Ferroelectr. Freq. Control **49**, 426–435 (2002).
[25]A. Sarvazyan, O. V. Rudenko, S. D. Swanson, J. B. Fowlkes, and S. Y. Emelianov, "Shear wave elasticity imaging a new ultrasonic technology of medical diagnostics," Ultrasound Med. Biol. **24**, 1419–1435 (1998).
[26]M. Tanter, J. Bercoff, A. Athanasiou, T. Deffieux, J.-L. Gennisson, G. Montaldo, M. Muller, A. Tardivon, and M. Fink, "Quantitative assessment of breast lesion viscoelasticity:Initial clinical results using supersonic shear imaging," Ultrasound Med. Biol. **34**, 1373–1386 (2008).
[27]J. R. McLaughlin, D. Renzi, K. J. Parker, and Z. Wu, "Shear wave speed recovery using moving interference patterns obtained in sonoelastography experiments," J. Acoust. Soc. Am. **121**, 2438–2446 (2007).
[28]K. Hoyt, B. Castaneda, and K. Parker, "Two-dimensional sonoelastographic shear velocity imaging," Ultrasound Med. Biol. **34**, 276–288 (2008).
[29]K. Hoyt, K. Parker, and D. Rubens, "Real-time shear velocity imaging using sonoelastographic techniques," Ultrasound Med. Biol. **33**, 1086–1097 (2007).
[30]K. Lin, J. R. McLaughlin, D. Renzi, and A. Thomas, "Shear wave speed recovery in sonoelastography using crawling wave data," J. Acoust. Soc. Am. **128**, 88–97 (2010).
[31]I. Shalem and I. Yavneh, "A multilevel graph algorithm for two dimensional phase unwrapping," Comput. Visualization Sci. **11**, 89–100 (2008).
[32]R. Anderssen and M. Hegland, "For numerical differentiation, dimensionality can be a blessing!," Math. Comput. **68**, 1121–1141 (1999).